Drug Design, Development and Therapy

Dovepress
open access to scientific and medical research

Open Access Full Text Article

ORIGINAL RESEARCH

Development and Characterization of a Novel Carbon-11 Labeled Positron Emission Tomography Radiotracer for Neuroimaging of Sirtuin 1 with Benzoxazine-Based Compounds

Yanli Wang[1], Yan Liu[1,2], Yongle Wang[1,3], Ping Bai[1], Madelyn Rose Hallisey[1], Breanna Lizeth Varela[1], Anne Siewko[1], Changning Wang[1], Yulong Xu[1]

[1]Athinoula A. Martinos Center for Biomedical Imaging, Department of Radiology, Massachusetts General Hospital, Harvard Medical School, Charlestown, MA, 02129, USA; [2]School of Pharmacy, Lanzhou University, Lanzhou, Gansu, 730000, People's Republic of China; [3]School of Pharmacy, Minzu University of China, Beijing, 100081, People's Republic of China

Correspondence: Yulong Xu; Changning Wang, Email Yulong.Xu@mgh.harvard.edu; cwang15@mgh.harvard.edu

Introduction: Sirtuins (SIRTs) comprise a group of histone deacetylase enzymes crucial for regulating metabolic pathways and contributing significantly to various disease mechanisms. Sirtuin 1 (SIRT1), among the seven known mammalian homologs, is extensively investigated and understood, playing a key role in neurodegenerative disorders and cancer. This study focuses on potential as a therapeutic target for conditions such as Parkinson's disease (PD), Huntington's disease (HD), and Alzheimer's disease (AD).

Methods: Utilizing positron emission tomography (PET) as a noninvasive molecular imaging modality, we aimed to expedite the validation of a promising sirtuin 1 inhibitor for clinical trials. However, the absence of a validated sirtuin 1 PET radiotracer impedes clinical translation. We present the development of [^{11}C]**1**, and ^{11}C-labeled benzoxazine-based derivative, as a lead imaging probe. The radiosynthesis of [^{11}C]**1** resulted in a radiochemical yield of 31 ± 4%.

Results: Baseline studies demonstrated that [^{11}C]**1** exhibited excellent blood-brain barrier (BBB) penetration capability, with uniform accumulation throughout various brain regions. Self-blocking studies revealed that introducing an unlabeled compound **1**, effectively blocking sirtuin 1, led to a substantial reduction in whole-brain uptake, emphasizing the in vivo specificity of [^{11}C]**1** for sirtuin 1.

Discussion: The development of [^{11}C]**1** provides a valuable tool for noninvasive imaging investigations in rodent models with aberrant sirtuin 1 expression. This novel radiotracer holds promise for advancing our understanding of sirtuin 1's role in disease mechanisms and may facilitate the validation of sirtuin 1 inhibitors in clinical trials.

Keywords: sirtuin 1, neuroimaging, benzoxazine-based derivative, blood-brain barrier

Introduction

Sirtuins, as nicotinamide adenine dinucleotide (NAD^+)-dependent deacetylases, play a pivotal role in deacetylating diverse protein substrates, including transcription factors and histones.[1] The broad involvement of sirtuins in numerous physiological processes highlights their significant biological relevance. Within the sirtuin family, comprised of seven known members (sirtuin 1–7), each subtype exhibits distinct localization and functions. Notably, sirtuin 1 has garnered substantial attention over the past two decades, primarily due to its association with increased longevity.[2] Extensive evidence suggests that sirtuin 1 plays a role in normal cell development, inflammatory responses, and energy metabolism, making it a potential therapeutic target for addressing age-related diseases, including neurodegenerative disorders and cancer.[3–5] To date, various chemical modulators targeting sirtuin 1 have been developed, encompassing both activators and inhibitors.

Sirtuin 1 (SIRT1) activators and inhibitors employ distinct mechanisms to modulate the activity and function of the SIRT1 enzyme. Activators enhance SIRT1's enzymatic activity by interacting with the enzyme, thereby increasing its binding affinity to substrates such as histones and other proteins. Additionally, some activators may induce the upregulation of SIRT1 expression,

Received: 10 October 2023
Accepted: 16 January 2024
Published: 15 March 2024

resulting in elevated enzyme levels. These actions contribute to physiological benefits, including improved metabolic function and potential longevity. Conversely, SIRT1 inhibitors suppress the enzymatic activity of SIRT1 by binding to its catalytic site, preventing the deacetylation of target proteins. The dynamic regulation of the SIRT1 enzyme by both activators and inhibitors influences various cellular pathways and processes in a context-dependent manner.[6] Sirtuin 1 activators, such as resveratrol and SRT1720, have demonstrated protective effects against conditions like diabetes, obesity-induced fatty liver, and insulin resistance. Nonetheless, several limitations hinder the practical applications of these activators, including rapid metabolism, low bioavailability, and their contentious mechanism of action on sirtuin 1.[7]

In the realm of clinical trials targeting sirtuin 1 (Sirt1), the leading contender is Selisistat (EX-527), recognized as a potent and selective Sirt1 inhibitor. Selisistat underwent rigorous evaluation in phase III clinical trials, with a specific emphasis on its potential efficacy in addressing Huntington's Disease.[8] Unfortunately, the clinical assessment yielded disappointing results, revealing no observable benefits within a brief treatment duration of 2 weeks. Currently, Selisistat stands as the sole Sirt1 inhibitor that has advanced to the advanced clinical stage of phase III trials.[9] Despite encountering limited success, continuous efforts persist in the quest for novel small molecule Sirt1 modulators. This ongoing research aims to identify compounds with heightened specificity for Sirt1, propelling the development of innovative therapeutic options. Consequently, the clinical advancement of Sirt1 inhibitors remains a dynamic area of investigation, with Selisistat serving as a pivotal milestone in progressing to advanced clinical trials, laying the groundwork for future exploration and therapeutic advancements in Sirt1 modulation.[10] Nevertheless, there is an urgent demand for next-generation modulators with enhanced specificity for sirtuin 1, particularly for their potential applications in clinical trials targeting diverse human diseases.[11]

Positron emission tomography (PET) is a noninvasive molecular imaging modality that offers the quantification and visualization of intricate biochemical processes.[12] PET imaging, utilizing radiotracers such as [^{18}F]-2--fluorobenzoylaminohexanoicanilide[13] and [^{11}C]WL-1,[14] enables noninvasive monitoring of SIRT1 expression activity. These radiotracers, specific to SIRT1, facilitate the visualization of its spatial and temporal dynamics in living organisms. Preclinical studies validated the use of SIRT1 inhibitors, such as EX-527, through PET imaging, demonstrating their potential in assessing the efficacy of SIRT1-targeted drugs. PET in mouse models of early-stage alcoholic liver disease revealed decreased [^{11}C]WL-1 uptake in affected organs, indicating its potential for studying diseases associated with altered SIRT1 activity. This approach could aid in clinical studies and the development of SIRT1-targeted therapies.

The creation of PET radiotracers specific to sirtuin 1 holds immense value, enabling an in-depth exploration of sirtuin 1's pathological implications and expediting the discovery of sirtuin 1 modulators. Tremendous efforts, including contributions from our research group, have been dedicated to developing sirtuin 1 PET radiotracers. Despite substantial progress, a validated sirtuin 1 PET radiotracer that meets the criteria for clinical translation remains elusive. Given our ongoing commitment to crafting PET tracers for the central nervous system (CNS), our current focus revolves around the development of brain-penetrating sirtuin 1 PET radiotracers poised for clinical utility.[15–17] This endeavor promises to provide the scientific community with essential imaging tools for monitoring sirtuin 1 within the human brain, both under pathological and healthy conditions. Such insights will significantly enhance our comprehension of how sirtuin 1 dysfunction contributes to various diseases, ultimately paving the way for novel therapeutic strategies aimed at modulating sirtuin 1. In this study, we embarked on the development of a PET tracer utilizing a lead compound known as 1, aptly named "Sosbo" for "sirtuin one selective benzoxazine" (Figure 1).[18] Compound **1**, selected from the existing literature, presented an ideal candidate due to the presence of a cyano group, which facilitates carbon-11 labeling. Notably, this compound boasts an IC_{50} value of 220 nM against sirtuin 1, indicating its potent affinity, while exhibiting considerably lower affinities of 37.7 μM toward sirtuin 2 and >60 μM toward sirtuin 3. These findings were derived from a novel lysine deacetylase assay employing firefly luciferase acetylated at the active site lysine K529 (FLucK529ac) as the substrate. In the current investigation, our primary objectives were the radiolabeling of the benzoxazine-based compound **1** and the comprehensive evaluation of its sirtuin 1 binding characteristics, alongside other pertinent biochemical properties, within the rodent brain, all achieved through state-of-the-art PET imaging techniques.

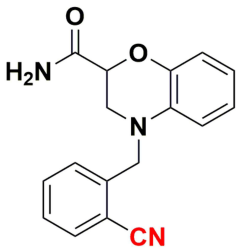

Compound 1

Sirtuin 1 IC_{50} = 220 nM
Sirtuin 2 IC_{50} = 37700 nM
Sirtuin 3 IC_{50} > 60000 nM

Figure 1 The Benzoxazine-Based Compound 1 Investigated in this Study: Carbon-11 PET Radiolabeling Position Highlighted in Red.

Materials and Methods

General

Reagents

Unless specifically noted, all reagents were employed as commercially sourced without the need for additional purification.

Animal Studies

The mouse-based investigations were conducted at Massachusetts General Hospital, operating under PHS Assurance of Compliance No. A3596-01. The Institutional Animal Care and Use Committee (IACUC) for Massachusetts General Hospital, represented by the Subcommittee on Research Animal Care (SRAC), meticulously reviewed and approved all procedures detailed within this manuscript.

Animal Housing and Care

For the well-being of the mice, all animals were housed socially in cages designed to cater to their physical and behavioral needs. They were afforded unrestricted access to both food and water and received supplementary nutritional support as prescribed by the attending veterinary staff. For this study, PET-CT imaging was performed on a total of four 6-month-old male C57BL/6 mice, exhibiting weights within the range of 30.1 g to 33.5 g.

Chemistry

4-(2-Iodobenzyl)-3,4-dihydro-2H-benzo[b][1,4]oxazine-2-carboxamide (2, Precursor) [18]

A solution of 3,4-dihydro-2H-benzo[b][1,4]oxazine-2-carboxamide **(3)** (1.0 equiv.) in acetone was prepared. To this solution, 2-iodobenzyl bromide **(5)** (1.5 equiv.), NaI (0.1 equiv.), and K2CO3 (3.0 equiv.) were added, and the resulting mixture was stirred at 65 °C for 24 hours. Upon cooling to room temperature, the reaction mixture underwent filtration, followed by acetone washing, and subsequent solvent removal under reduced pressure. Purification through column chromatography (PE/EtOAc 2:1 to 1:1) yielded a colorless solid (50.0 mg, 22%).

4-(2-Cyanobenzyl)-3,4-dihydro-2H-benzo[b][1,4]oxazine-2-carboxamide (1, Reference) [18]

A solution of 3,4-dihydro-2H-benzo[b][1,4]oxazine-2-carboxamide **(3)** (1.0 equiv.) in acetone was prepared. To this solution, 2-(bromomethyl)-benzonitril **(4)** (1.5 equiv.), NaI (0.1 equiv.), and K_2CO_3 (3.0 equiv.) were added. The resulting suspension was stirred at 65 °C for 5 hours. After cooling to room temperature, the reaction mixture was filtered, followed by acetone washing, and subsequent solvent removal under reduced pressure. Purification by column chromatography (PE/EtOAc 2:1 to 1:1) resulted in the isolation of a colorless solid (94.0 mg, 57%).

Radiosynthesis of [^{11}C]1

[^{11}C]CO_2 was produced via the 14N (p, α) ^{11}C reaction on nitrogen containing 2.5% oxygen, using 11 MeV protons from a Siemens Eclipse cyclotron. The [^{11}C]CO_2 was then trapped on molecular sieves within a TRACERlab FX-MeI synthesizer (General Electric).

[^{11}C]CH_4 was generated through the reduction of [^{11}C]CO_2 in the presence of Ni/hydrogen at 350 °C. This [^{11}C]CH_4 subsequently reacted with NH_3 on Pt at 900 °C, resulting in the production of [^{11}C]HCN. Helium was employed as the carrier gas throughout this process. The prepared [^{11}C]HCN was directly introduced into the reaction vial.

In the reaction vessel, [^{11}C]HCN was trapped in anhydrous DMSO (300 μL) alongside precursor **2** (1.0 mg), Pd$(PPh_3)_4$ (3.5 mg), and K_2CO_3 (4.0 mg). The reaction mixture was heated to 110 °C and maintained at this temperature for 5 minutes. Subsequently, the radioactive mixture containing [^{11}C]**1** was quenched by adding an HPLC mobile phase (0.7 mL) and then injected into a reverse-phase semipreparative HPLC system (Phenomenex Gemini-NX 5u C18 110A, 250×10 mm, 5.0 mL/min). A gradient of 10–90% CH_3CN in H_2O was used for elution.

A radioactive fraction with a retention time of approximately 11 minutes was collected into a flask and diluted in water (30 mL). The final product was reconstituted by passing it through a solid-phase exchange (SPE) C-18 cartridge (Waters WAT020515 Sep-Pak Plus Short C18). The cartridge was rinsed with water (4 × 5 mL), and the product was eluted with EtOH (0.3 mL) before being diluted with saline (2.7 mL).

To ensure the chemical and radiochemical purity of the final product, analytical HPLC (VARIAN Pursuit XRs 5 C18, 150×4.6 mm) was utilized. The elution gradient consisted of 10–90% CH_3CN in H_2O containing 0.1% TFA, at a flow rate of 2 mL/min.

The identity of [^{11}C]**1** was confirmed by co-injecting it with compound **1** as a reference standard (Figure S3). The determination of molar activity was accomplished by comparing the mass (μmol) of [^{11}C]**1** with known radioactivity through HPLC analysis, comparing UV absorbance at 254 nm to that of known concentrations of non-radioactive compound **1**.

Log $D_{7.4}$ Determination

To assess the partitioning behavior of the radiotracer [^{11}C]**1**, a mixture of 1-octanol and 0.2 M phosphate buffer (pH = 7.4) was employed. Specifically, the formulated PET tracer (150–200 μL, ~10.0 MBq) was vigorously mixed with 0.2 M phosphate buffer (2 mL, pH 7.4) and 1-octanol (2 mL) for 1 minute using a vortex apparatus. Following this mixing, a settling period of 1 hour was observed, during which three 100 μL samples were extracted from each layer. These extracted samples were then subjected to radioactivity measurement, and the log D7.4 values were calculated using the formula: $\log D7.4 = \log\left(A_{oct}/A_{phosphate\ buffer}\right)$, where A_{oct} and $A_{phosphate\ buffer}$ represent the average radioactivity levels from the three samples in the 1-octanol and phosphate buffer layers, respectively. The reported results are presented as mean values ± standard deviation.

PET/CT Acquisition and Post Processing

In this study, PET/CT imaging was conducted in male C57BL/6 mice with an average weight of 30–35 grams. A total of 2 mice were included for the baseline imaging group, and another 2 for the blocking study with pre-treatment of compound **1**. Prior to imaging, all mice were anesthetized using inhalational isoflurane, initially administered at 3% in a carrier of 2 L/min medical oxygen and subsequently maintained at 2% isoflurane for the duration of the scan. Animal safety during procedures was closely monitored by experienced animal technicians.

The mice were securely positioned in a prone orientation on the bed of a Triumph Trimodality PET/CT scanner (Gamma Medica, Northridge, CA). [^{11}C]**1** (150–200 μL, ~5.0 MBq) was administered via lateral tail vein catheterization at the commencement of the PET scan. In the case of blocking studies, compound **1** (3 mg/kg, iv) was injected 10 minutes prior to the administration of [^{11}C]**1**.

The dynamic PET acquisition extended over a 60-minute period and was succeeded by CT imaging for anatomical co-registration. PET data were subjected to reconstruction employing a 3D-MLEM method, resulting in a full width at half-maximum resolution of 1 mm. Corrections for uniformity, scatter, and attenuation were duly applied.

Reconstructed images, together with an anatomical CT scan, were exported from the scanner in DICOM format. Subsequently, these files were imported into the PMOD 3.2 software (PMOD Technology, Zurich, Switzerland) for further analysis.

PET/CT Image Analysis

For the analysis of PET images, we employed the PMOD 3.2 software (PMOD Technology, Zurich, Switzerland). Volumes of interest (VOIs) were manually delineated as spherical regions of interest. The VOI placement was guided by high-resolution CT structural images and summed PET data. To minimize partial volume effects, the chosen radius for each sphere was no less than 1 mm.

The time-activity curves (TACs) were subsequently generated, providing decay-corrected activity values at specified time points with intervals that progressively increased. This approach allowed for a comprehensive evaluation of radiotracer kinetics over the course of the study.

Results and Discussion

The synthesis of compound **1** and its corresponding labeling precursor **2** was carried out following a previously reported method (Scheme 1).[18] The reaction of 3,4-dihydro-2H-benzo[b][1,4]oxazine-2-carboxamide **(3)** with 2-iodobenzyl bromide **(5)** yielded benzo-xazine-based derivative 2 with a 72% yield. The coupling of compound 3 with 2-(bromomethyl)-benzonitrile **(4)** resulted in the reference compound 1 with a 57% yield. The PET tracer [^{11}C]**1** was synthesized via Pd-mediated cyanation using [^{11}C]HCN (Scheme 2). Precursor **2** was treated with [^{11}C]HCN and $Pd(PPh_3)_4$ in

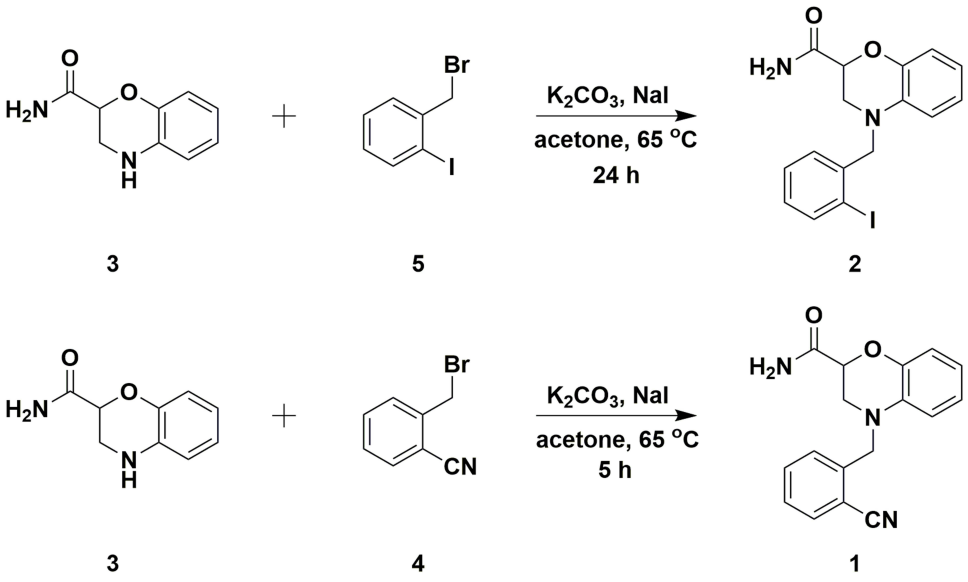

Scheme 1 Synthesis of the benzoxazine-based compound **1** and the labeling precursor **2**.

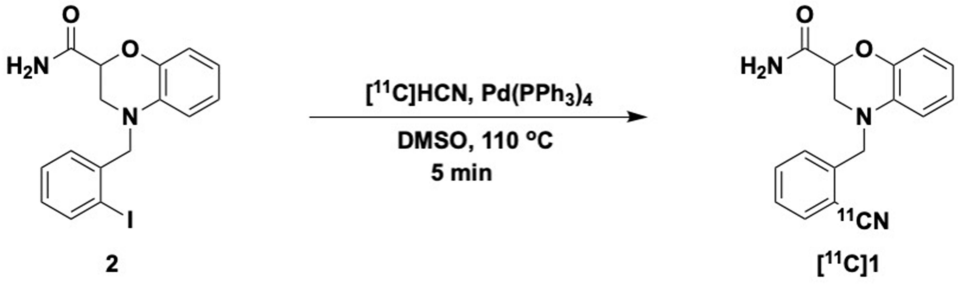

Scheme 2 One-step radiosynthesis of [^{11}C]**1**.

anhydrous DMSO at 110 °C for 5 minutes, and [^{11}C]**1** was purified by HPLC, providing a radiochemical yield of 31 ± 4% (based on [^{11}C]HCN, decay-corrected to the start of synthesis) within a total synthesis time of 30 minutes (see Figure S1). Following formulation, [^{11}C]**1** was obtained with a radiochemical purity exceeding 99% (see Figure S2) and a molar activity of 312 ± 85 GBq/μmol (n = 3). Subsequently, the distribution coefficients of [^{11}C]**1** at physiological pH (log D7.4) were determined using the shake flask method, revealing a log D7.4 value of 2.03 ± 0.05 (n = 3). This log D7.4 value falls within the typical range for small molecules that exhibit good brain penetration. Scheme 1. Synthesis of the benzoxazine-based compound **1** and the labeling precursor **2**.

Following the successful and reliable synthesis of [^{11}C]**1**, PET/CT scanning was conducted to assess its biological properties. Initially, C57BL/6 mice were employed to investigate the biodistribution of [^{11}C]**1**. Representative brain PET/CT images and time-activity curves (TACs) in Figure 2A–D illustrates that [^{11}C]**1** displayed robust blood-brain barrier (BBB) penetration capabilities and homogeneous accumulation within brain regions. [^{11}C]**1** exhibited substantial brain uptake, reaching a peak signal of approximately 2.2 SUV in the whole brain at 1 minute post-injection. By 10 minutes post-injection, the signal experienced a rapid decline to approximately 0.9 SUV. Notably, the observed brain uptake of [^{11}C]**1** aligns with the calculated CNS MPO score of 5.5 (a qualitative measuring algorithm for predicting brain uptake).[19] Furthermore, the brain uptake was consistent with the CNS PET MPO score of 4 for [^{11}C]**1** (the maximum CNS PET MPO score is 6, with the threshold typically defined as ≥ 3).

It is noteworthy that radioactivity in all tissues of interest exhibited rapid decreases after the initial uptake, while the signals in the liver and kidney remained notably high (Figure 2E, 7.4 SUV and 6.3 SUV at 60 minutes post-injection, respectively). The radioactivity of [^{11}C]**1** displayed low uptake in the blood, followed by a swift washout (3.2 SUV at 5 minutes and 0.8 SUV at 60 minutes). Muscle tissue exhibited the lowest level of radioactivity (< 0.4 SUV). Liver and kidney demonstrated the highest uptakes (> 4.6 SUV), indicating rapid urinary and hepatobiliary elimination of [^{11}C]**1**.

To determine specific binding toward sirtuin 1 in the mouse brain, we next performed blocking studies by pre-treating with unlabeled compound **1** (3 mg/kg, iv), 10 min prior to the [^{11}C]**1** administration in mice (Figure 3). As we know, the radioactivity signal will be decreased if unlabeled compound competes with the PET probe toward binding with target, which demonstrates specific binding.[20] However, the TACs of self-blocking studies indicated remarkably increased total uptake of [^{11}C]**1** in the whole brain relative to baseline studies (Figure 3A). These results indicated that the whole-body binding sites blocked by unlabeled compound **1** might lead to the increased levels of free radiotracer [^{11}C]**1** in plasma, which would result in a brain SUV increase during the entire scan time. Therefore, normalization of whole brain radioactivities in baseline and self-blocking studies to their maximal blood radioactivity levels were performed to evaluate the specific binding of [^{11}C]**1**. As shown in Figure 3B, blocking of sirtuin 1 with unlabeled compound **1** resulted in a significant decrease in the whole brain uptake (~35% reduction based on area under curve, AUC), which demonstrated good in vivo specificity of [^{11}C]**1** toward sirtuin 1.

To assess specific binding to sirtuin 1 in the mouse brain, we conducted blocking studies by administering unlabeled compound **1** (3 mg/kg, iv) to mice 10 minutes before the administration of [^{11}C]**1** (Figure 3). As known, the radioactivity signal decreases if unlabeled compound competes with the PET probe for binding to the target, demonstrating specific binding.[20] However, the time-activity curves (TACs) from self-blocking studies indicated a significant increase in the total uptake of [^{11}C]**1** in the whole brain compared to baseline studies (Figure 3A). These results suggest that blocking whole-body binding sites with unlabeled compound 1 might lead to elevated levels of free radiotracer [^{11}C]**1** in plasma, resulting in increased brain SUV throughout the entire scan. Therefore, we normalized whole brain radio activities in baseline and self-blocking studies to their respective maximal blood radioactivity levels to evaluate the specific binding of [^{11}C]**1**. As shown in Figure 3B, blocking sirtuin 1 with unlabeled compound **1** led to a substantial reduction in whole-brain uptake (approximately 35% reduction based on area under the curve, AUC), demonstrating the strong in vivo specificity of [^{11}C]**1** for sirtuin 1.

The successful synthesis and comprehensive biological assessment of the PET tracer [^{11}C]**1** targeting sirtuin 1 set the stage for a detailed exploration of its applications. The multi-step synthesis, outlined in Scheme 1, yielded high efficiencies for compounds 1 and 2. Subsequent [^{11}C]**1** synthesis via Pd-mediated cyanation proved efficient, with a 31 ± 4% radiochemical yield in just 30 minutes. The resulting radiotracer demonstrated exceptional purity (>99%) and a molar activity of 312 ± 85 GBq/μmol, crucial for precise imaging. The log D7.4 value of 2.03 ± 0.05, indicative of

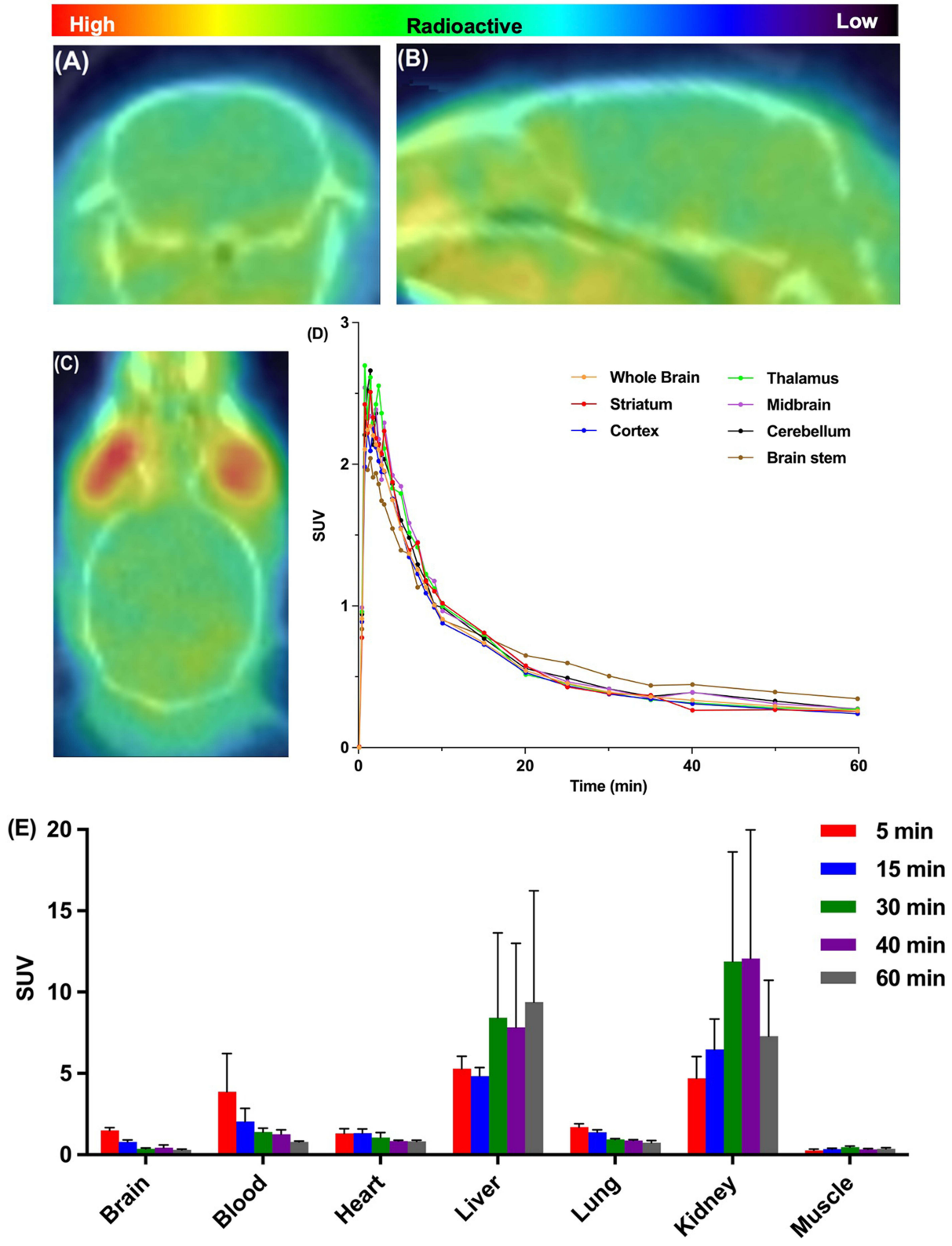

Figure 2 Baseline Studies of [^{11}C]**1** in C57BL/6 Mice. (**A**) Representative PET Transverse Image in Mouse Brain (Summed 30–60 min). (**B**) Representative PET Sagittal Image in Mouse Brain (Summed 30–60 min). (**C**) Representative PET Coronal Image in Mouse Brain (Summed 30–60 min). (**D**) Time-Activity Curves (TACs) in Six Representative Mouse Brain Regions and Whole Brain. All Data Are the Mean. (**E**) Whole Body Biodistribution Histogram at Five Different Time Points (5, 15, 30, 40, and 60 min) post-Injection. All Data Are the Mean ± SD. The Radioactivity Accumulation Is Presented as the Standardized Uptake Value (SUV).

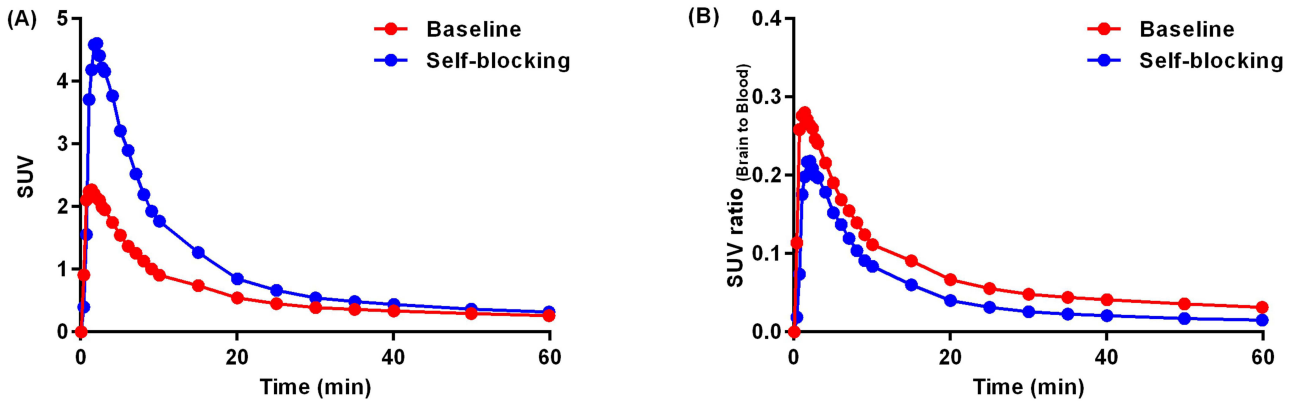

Figure 3 Time-Activity Curves (TACs) of Baseline and Self-Blocking Experiments in C57BL/6 Mouse Brains. (**A**) TACs for the Whole Brain. All data represent the mean and radioactivity accumulation is expressed as the standardized uptake value (SUV). (**B**) Normalized Whole Brain TACs Relative to Maximal Blood Radioactivities. All data represent the mean.

favorable brain penetration, further underscores [^{11}C]**1** 's neuroimaging potential. PET/CT scans in C57BL/6 mice revealed [^{11}C]**1** 's robust blood-brain barrier penetration and homogeneous brain accumulation, making it a promising candidate for in vivo sirtuin 1 investigation. Achieving a peak signal of approximately 2.2 SUV within 1-minute post-injection, in line with calculated CNS MPO and CNS PET MPO scores, emphasizes its neuroimaging potential. The observed rapid brain signal decline post-injection indicates efficient washout, crucial for precision. Biodistribution analysis showed rapid radioactivity decreases post-initial uptake, with notable signals in the liver and kidney (>4.6 SUV), suggesting rapid elimination. Despite favorable characteristics, long-term imaging studies and dosimetry implications require consideration. Investigating [^{11}C]**1** 's specific binding to sirtuin 1 in mouse brains via blocking studies revealed the anticipated decrease in radioactivity. Unexpectedly, self-blocking studies showed increased total uptake, suggesting unlabeled compound 1 might block whole-body binding sites, elevating free [^{11}C]**1** in plasma and subsequently increasing brain SUV. Normalization to maximal blood radioactivity levels highlighted a substantial (~35%) reduction in whole-brain uptake during sirtuin 1 blocking studies, underscoring [^{11}C]**1** 's robust in vivo specificity for sirtuin 1.

Conclusions

In this study, we successfully developed and assessed a novel PET tracer targeting sirtuin 1 in healthy C57BL/6 mice. The radiotracer [^{11}C]**1** exhibited excellent blood-brain barrier penetration and demonstrated specific binding to sirtuin 1 in vivo. This finding provides a valuable tool for conducting quantitative imaging studies in rodent models with aberrant sirtuin 1 expression. [^{11}C]**1** can be regarded as a promising sirtuin 1 specific radio probe, enabling in-depth investigations into the role of sirtuin 1 in the pathogenesis of aging-related diseases and offering insights into potential sirtuin 1-based therapeutic interventions for age-related conditions. Future studies in higher animal species will be explored and detailed in upcoming publications.

Ethics Statement

Compliance with ethical standards.

Acknowledgments

We extend our gratitude to the dedicated staff at the Martinos Center for their invaluable assistance with radiosynthesis and rodent experiments. This work received generous support from the National Institutes of Health (NIH) under grant AG015379 (C.W.). The imaging studies were conducted at the Athinoula A. Martinos Center for Biomedical Imaging at Massachusetts General Hospital, utilizing resources made available by the Center for Functional Neuroimaging Technologies, P41EB015896, a P41 Regional Resource generously supported by the National Institute of Biomedical Imaging and Bioengineering (NIBIB), part of the NIH.

We would also like to acknowledge the instrumental role played by NIH Shared Instrumentation Grant Program and High-End Instrumentation Grant Program, specifically grant numbers: S10OD025234, S10RR017208, S10RR026666, S10RR022976, S10RR019933, S10RR023401, and S10OD023517, in providing access to the necessary instrumentation for this research.

Disclosure

The authors declare no competing interests in this work.

References

1. Jing H, Lin H. Sirtuins in epigenetic regulation. *Chem Rev*. 2015;115(6):2350–2375. doi:10.1021/cr500457h
2. Cantó C, Auwerx J. Caloric restriction, SIRT1 and longevity. *Trends Endocrinol Metab*. 2009;20(7):325–331. doi:10.1016/j.tem.2009.03.008
3. Herskovits AZ, Guarente L. SIRT1 in neurodevelopment and brain senescence. *Neuron*. 2014;81(3):471–483. doi:10.1016/j.neuron.2014.01.028
4. O'Callaghan C, Vassilopoulos A. Sirtuins at the crossroads of stemness, aging, and cancer. *Aging Cell*. 2017;16(6):1208–1218. doi:10.1111/acel.12685
5. Fujita Y, Yamashita T. Sirtuins in neuroendocrine regulation and neurological diseases. *Front Neurosci*. 2018;12:778. doi:10.3389/fnins.2018.00778
6. Timmers S, Konings E, Bilet L, et al. Calorie restriction-like effects of 30 days of resveratrol supplementation on energy metabolism and metabolic profile in obese humans. *Cell Metab*. 2011;14(5):612–622. doi:10.1016/j.cmet.2011.10.002
7. Marcotte PA, Richardson PL, Guo J, et al. Fluorescence assay of SIRT protein deacetylases using an acetylated peptide substrate and a secondary trypsin reaction. *Anal Biochem*. 2004;332(1):90–99. doi:10.1016/j.ab.2004.05.039
8. Pacholec M, Bleasdale JE, Chrunyk B, et al. SRT1720, SRT2183, SRT1460, and resveratrol are not direct activators of SIRT1. *J Biol Chem*. 2010;285(11):8340–8351. doi:10.1074/jbc.M109.088682
9. Dai H, Kustigian L, Carney D, et al. SIRT1 activation by small molecules-kinetic and biophysical evidence for direct interaction of enzyme and activator. *J Biol Chem*. 2010;285(43):32695–32703. doi:10.1074/jbc.M110.133892
10. Süssmuth SD, Haider S, Landwehrmeyer GB, et al. An exploratory double-blind, randomized clinical trial with selisistat, a SirT1 inhibitor, in patients with Huntington's disease. *Br J Clin Pharmacol*. 2015;79(3):465–476. doi:10.1111/bcp.12512
11. Broussy S, Laaroussi H, Vidal M. Biochemical mechanism and biological effects of the inhibition of silent information regulator 1 (SIRT1) by EX-527 (SEN0014196 or selisistat). *J Enzyme Inhib Med Chem*. 2020;35(1):1124–1136. doi:10.1080/14756366.2020.1758691
12. Suridjan I, Comley RA, Rabiner EA. The application of positron emission tomography (PET) imaging in CNS drug development. *Brain Imaging Behav*. 2019;13(2):354–365. doi:10.1007/s11682-018-9967-0
13. Bonomi R, Popov V, Laws MT, et al. Molecular imaging of sirtuin1 expression-activity in rat brain using positron-emission tomography-magnetic-resonance imaging with [^{18}F]-2-fluorobenzoylaminohexanoicanilide. *J Med Chem*. 2018;61(16):7116–7130. doi:10.1021/acs.jmedchem.8b00253
14. Xu Y, Chen Z, Wey H-Y, et al. Molecular imaging of NAD^+-dependent deacetylase SIRT1 in the brain. *Alzheimers Dement*. 2021;17(12):1988–1997. doi:10.1002/alz.12344
15. Chen Z, Wang X, Xu Y, Wang C. Synthesis of ^{11}C-labeled DNA polymerase-β inhibitor 5-methoxyflavone and PET/CT imaging thereof. *Nucl Med Biol*. 2019;78–79:17–22. doi:10.1016/j.nucmedbio.2019.10.005
16. Xu Y, Wang Y, Wang H, Wang C. Synthesis and characterization of carbon-11 labeled iloperidone for imaging of α_1-adrenoceptor in brain. *Front Mol Biosci*. 2020;7:586327. doi:10.3389/fmolb.2020.586327
17. Xu Y, Wang C, Wey H-Y, et al. Molecular imaging of Alzheimer's disease-related gamma-secretase in mice and nonhuman primates. *J Exp Med*. 2020;217(12):e20182266. doi:10.1084/jem.20182266
18. Spinck M, Bischoff M, Lampe P, Meyer-Almes F-J, Sievers S, Neumann H. Discovery of dihydro-1,4-benzoxazine carboxamides as potent and highly selective inhibitors of sirtuin-1. *J Med Chem*. 2021;64(9):5838–5849. doi:10.1021/acs.jmedchem.1c00017
19. Wager TT, Hou X, Verhoest PR, Villalobos A. Moving beyond rules: the development of a central nervous system multiparameter optimization (CNS MPO) approach to enable alignment of drug-like properties. *ACS Chem Neurosci*. 2010;1(6):435–449. doi:10.1021/cn100008c
20. Van de Bittner GC, Ricq EL, Hooker JM. A philosophy for CNS radiotracer design. *Acc Chem Res*. 2014;47(10):3127–3134. doi:10.1021/ar500233s